



PCCP

**Oxide-ion diffusion in brownmillerite-type $\text{Ca}_2\text{AlMnO}_{5+\delta}$
from first-principles calculations**

Journal:	<i>Physical Chemistry Chemical Physics</i>
Manuscript ID	CP-ART-11-2021-005174
Article Type:	Paper
Date Submitted by the Author:	12-Nov-2021
Complete List of Authors:	Matsumoto, Ushio; Japan Fine Ceramics Center, Nanostructures Research Lab. Kuwabara, Akihide; Japan Fine Ceramics Center, Nanostructures Research Laboratory Fisher, Craig; Japan Fine Ceramics Center, Nanostructures Research Laboratory Moriwake, Hiroki; Japan Fine Ceramics Center, Nanostructures Research Laboratory Tanaka, Isao; Kyoto University, Materials Science and Engineering

SCHOLARONE™
Manuscripts

Oxide-ion diffusion in brownmillerite-type $\text{Ca}_2\text{AlMnO}_{5+\delta}$ from first-principles calculations

Ushio Matsumoto,^{*a,b,c} Akihide Kuwabara,^{**a} Craig A. J. Fisher,^a Hiroki Moriwake^a and Isao Tanaka^{a,c}

^a Nanostructures Research Laboratory, Japan Fine Ceramics Center, 2-4-1 Mutsuno, Atsuta-ku, Nagoya 456-8587, Japan.

^b Digital Innovation Center, Furukawa Electric Co., Ltd., 4-3 Okano 2, Nishi-ku, Yokohama 220-0073, Japan.

^c Department of Materials Science and Engineering, Kyoto University, Kyoto 505-8501, Japan.

* Email: ushio_matsumoto@jfcc.or.jp

** Email: kuwabara@jfcc.or.jp

Keywords

Oxide-ion conductivity, oxygen storage material, brownmillerite oxide

Abstract

Oxide-ion diffusion pathways in brownmillerite oxides $\text{Ca}_2\text{AlMnO}_5$ and $\text{Ca}_2\text{AlMnO}_{5.5}$ are systematically investigated using first-principles calculations. These structures reversibly transform into each other by oxidation and reduction. We examine oxide-ion migration in $\text{Ca}_2\text{AlMnO}_5$ and $\text{Ca}_2\text{AlMnO}_{5.5}$ using the nudged elastic band method. In the reduced structure ($\text{Ca}_2\text{AlMnO}_5$), oxide-ion migration through a vacancy channel is found to have the lowest migration energy barrier, at 0.58 eV. The migration energy barrier of the second-lowest energy path, perpendicular to the vacancy channel, is found to be 0.98 eV. In the oxidized structure ($\text{Ca}_2\text{AlMnO}_{5.5}$), oxide-ion migration within AlO_6 layers has migration energy barriers of 0.55 eV and 0.56 eV in the [100] and [001] directions, respectively. Oxide-ion migration perpendicular to the AlO_6 layer has a migration energy barrier of 1.33 eV, suggesting that oxide-ion diffusion in the [010] direction is difficult even at elevated temperature. These results indicate that diffusion in the reduced phase is predominantly one-dimensional whereas it is two-dimensional in the oxidized phase.

Introduction

Brownmillerite (BM) oxides that exhibit high oxide-ion conductivity are promising functional materials for a range of applications. BM oxides have the general formula $A_2B_2O_5$, where A and B are divalent alkaline earth and trivalent transition metals, respectively. Some BM oxides are capable of being reversibly transformed into a perovskite form, $ABO_{3-\delta}$, by oxidation, applying high pressure, or heating to high temperatures.^{1,2} The first of these structural transformations is a topotactic phase transition. Because the structural changes are accompanied by changes in physical and chemical properties such as electronic conductivity, magnetic susceptibility, and ionic transport, numerous studies have been carried out to determine the mechanism of the topotactic phase transition and its influence on these properties.

Oxide-ion transport is of enormous research interest because it is the key property in many applications, such as solid oxide fuel cells (SOFC),³⁻⁵ oxygen storage materials (OSM),⁶⁻⁸ oxygen gas sensors and, more recently, the electronically insulating layer in resistive-switching random access memory^{9,10}. Consequently, a great deal of effort has been expended to elucidate the relationship between oxide-ion diffusion, composition and crystal structure in this family of materials.^{5,9-13} For example, the importance of vacancy channels in BM oxides has been highlighted by van Doorn et al.,⁵ who reported a possible diffusion pathway in $La_{1-x}Sr_xCoO_{3-\delta}$ based on high-resolution transmission electron microscopy observations. According to first-principles calculations by Mitra et al.,¹² the energy barrier for oxide-ion migration along vacancy channels is ca. 0.6 eV in $SrCoO_{2.5}$, whereas perpendicular to the vacancy channels it is higher than 1.8 eV. These studies suggest that one-dimensional diffusion through vacancy channels dominates in Co-containing BM oxides. On the other hand, Shiiba et al.,⁹ based on results of molecular dynamics simulations with empirical potentials, reported that perovskite-type $(Ba_{0.5}Sr_{0.5})CoO_{2.5}$ and $(Ba_{0.5}Sr_{0.5})(Co_{0.8}Fe_{0.2})O_{2.5}$ exhibit two-dimensional and three-dimensional diffusion, respectively. Zhang et al.¹⁴ also reported that oxide ions in BM-type $SrCoO_{2.5}$ diffuse via two diffusion pathways parallel to $[110]$ and $[011]$ based on scanning transmission electron microscopy observations when $SrCoO_{2.5}$ is reduced to $SrCoO_2$. Since BM

oxides have a similar structural framework to the perovskites, it is reasonable to expect them to exhibit similar anisotropy in their properties.

Of the known BM oxides, cation-ordered $\text{Ca}_2\text{AlMnO}_{5+\delta}$ (CAMO) has received significant attention because it is a leading candidate for use as an OSM with high oxygen-storage capacity. According to experiments by Motohashi et al.,¹⁵ the oxygen capacity of CAMO is 3.0 wt%, which is equivalent to 90 % of the theoretical value (3.3 %). This value is 1.3 times larger than that of the best-known OSMs, materials in the $\text{ZrO}_2\text{--CeO}_2$ system, in commercial use. One important advantage of CAMO compared to other candidate materials with a high oxygen-storage capacity is that its constituents are all abundant elements in earth's crust, whereas some candidates,^{7,16,17} such as $\text{YBaCo}_4\text{O}_{7+\delta}$, $\text{Ce}_{0.5}\text{M}_{0.5}\text{O}_{2+\delta}$ ($\text{M} = \text{Zr}$ and Hf) and $\text{BaYMn}_2\text{O}_{5+\delta}$, contain rare-earth metals that are much less abundant. Furthermore, release and absorption of oxygen in CAMO is highly sensitive to variations in temperature. Despite these advantages and the interest in CAMO for a wide range of applications, few reports have examined the diffusion mechanism at the atomic level, particularly from a theoretical viewpoint.⁶

In this study, we investigate the oxygen diffusion mechanisms in CAMO in the oxidized and reduced states of CAMO. We begin our study by determining possible intermediate states and elementary migration paths in the structures of the two phases. We then perform first-principles calculations of oxide-ion transport via a number of candidate mechanisms using density functional theory (DFT).

Calculation methods

First-principles calculations of $\text{Ca}_2\text{AlMnO}_5$ and $\text{Ca}_2\text{AlMnO}_{5.5}$ were carried out using the projector augmented wave (PAW) method¹⁸ within the framework of DFT as implemented in the Vienna Ab initio Simulation Package (VASP)^{19,20}. The generalized gradient approximation (GGA) functional of Perdew–Burke–Ernzerhof parameterization adapted for solids (PBEsol)^{21,22} was used to treat the exchange-correlation interactions. Brillouin zone (BZ) integration was performed using a Monkhorst-Pack \mathbf{k} -point mesh,²³ with \mathbf{k} -point spacing of no more than 0.5 \AA^{-1} , and a

Gaussian smearing approach, with a smearing width of 0.01 eV. The cut-off energy for plane-wave basis sets was set at 500 eV. The $2s$ and $2p$ orbitals for O atoms, $3s$, $3p$ and $4s$ orbitals for Ca atoms, $3s$ and $3p$ orbitals for Al atoms, and $3p$, $4s$ and $3d$ orbitals for Mn atoms were treated as valence states. Atomic positions were fully optimized until all residual forces became less than 0.02 eV/Å. To treat the strongly correlated electrons of Mn reliably, an on-site Coulomb correction with an effective Hubbard parameter, U_{eff} , of 4.3 eV was applied to Mn $3d$ states. All Mn atoms were arranged in a ferro-magnetic (FM) configuration.

The effective Hubbard parameter for Mn was calculated based on the linear response method developed by Cococcioni et al.²⁴ Here, we used a $2 \times 1 \times 2$ (144-atom) supercell of the reduced structure. We set a more stringent energy convergence criterion than that used for atomic relaxation calculations; in this case, BZ integration was performed using a $4 \times 3 \times 4$ Γ -centered \mathbf{k} -point mesh and tetrahedron method with Blöchl corrections.

Simulated annealing was performed on both compounds by performing first-principles molecular dynamics simulations in the NVT ensemble with a time step of 2 fs at a temperature of 500 K for 10 ps (5000 time steps), followed by incremental lowering of the temperature to 100 K over 10 ps (5000 time steps). We used the Nosé–Hoover thermostat^{25,26} to control the temperature and the velocity–Verlet algorithm to integrate the equations of motion.

Various possible elementary oxide-ion migration paths were considered for interstitial, interstitialcy and vacancy diffusion mechanisms, where the jump distance was restricted to within the range of the neighbouring channels. Candidate pathways were generated by connecting one local minimum state to a neighbouring local minimum state. The energy surfaces of these paths were probed using the nudged elastic band (NEB) method.²⁷ To examine the dependence of the calculated migration energy barriers on supercell size, calculations were performed using both a $2 \times 1 \times 2$ (144-atom) supercell and a $3 \times 1 \times 3$ (324-atom) supercell of the reduced structure. Based on the results of this, $2 \times 2 \times 2$ (304-atom) and $3 \times 1 \times 3$ (324-atom) supercells were used to evaluate the migration energy barriers in the oxidized and reduced structures, respectively. When relaxing supercell models, atomic positions were fully optimized

until the residual forces were less than 0.02 eV/\AA , with the lattice constant fixed to that of the perfect crystals. All crystal images were generated using the VESTA program.²⁸

Results and discussion

Structures of $\text{Ca}_2\text{AlMnO}_5$ and $\text{Ca}_2\text{AlMnO}_{5.5}$

The unit cell of $\text{Ca}_2\text{AlMnO}_{5.5}$ (space group *Imma*) contains oxygen sites with fractional occupancies,²⁹ whereas all oxygen sites in $\text{Ca}_2\text{AlMnO}_5$ are fully occupied.³⁰ To determine the stable configuration of oxygen atoms in $\text{Ca}_2\text{AlMnO}_{5.5}$, we constructed four models, as illustrated in Fig. S1 in the supplementary information, and relaxed them using VASP. The results in supplementary information Table S1 show that the energies of structures C and D are about 0.28 eV per formula unit lower than that of structures A and B, suggesting that there is a small preference for O and Al atoms to form a zigzag chain in $\text{Ca}_2\text{AlMnO}_{5.5}$. The energies of structures C and D are the same within the limits of accuracy of the calculations. We thus selected structure D as the ground state of $\text{Ca}_2\text{AlMnO}_{5.5}$ when investigating the oxide-ion migration mechanism.

Simulated annealing of both compounds produced structures in good agreement with the initial structures optimized at 0 K , with total energies within 3 meV , giving us confidence that the structures correspond to the global minima for each composition.

Calculated lattice constants for $\text{Ca}_2\text{AlMnO}_5$ and $\text{Ca}_2\text{AlMnO}_{5.5}$ are compared with literature values²⁹⁻³¹ from both experiment and computational studies in Table 1. They show good agreement with reported values with errors of less than 2% .^{29,30} Calculated positional parameters for both structures are summarized in Tables S2 and S3 in the supplementary information.

When CAMO is oxidized, one $3d$ electron is removed from each Mn ion, resulting in the formal valence of Mn ions changing from $+3$ to $+4$. Experimental observations using electron energy-loss spectroscopy by Saito et al.³¹ is consistent with this change in charge state. Accordingly, the magnetic moments of Mn also change from 3.67 to 2.97 .

Migration energy barriers and the effect of cell size

According to the Arrhenius equation, the diffusion coefficient D is given by

$$D(T) = D_0 \exp\left(-\frac{E_a}{k_B T}\right) \quad ()$$

where D_0 , T and k_B represent the prefactor, temperature and Boltzmann constant, respectively, and E_a is the activation energy. D_0 depends on the jump frequency for an atom and is generally assumed to be independent of temperature. Conversely, the exponential term, which includes the activation energy, strongly depends on the temperature, so that a lower E_a results in a higher D at a given T . The activation energy is commonly expressed as the sum of the defect formation energy and the migration energy barrier, E_m . The preferential path for oxygen transport is identified by comparing the lowest E_m for different pathways.

The migration energy barrier of a path can be calculated using the NEB method, which is a method for finding saddle points and minimum energy paths between initial and final states on the energy surface. In this study, we examined the elementary migration paths of an excess oxygen atom in the oxidized and reduced structures. To evaluate the effect of supercell size on the calculated migration energy barrier, tests were performed for oxide-ion migration in the [001] direction of the reduced structure using different sized supercells. The calculated saddle points of the obtained energy paths in Fig. 2 show that the migration energy barriers in the $2 \times 1 \times 2$ and $3 \times 1 \times 3$ supercells are 0.51 eV and 0.58 eV, respectively. This difference in energy is small and both energy surfaces have a similar shape. A $2 \times 1 \times 2$ supercell was thus deemed sufficient for the remaining NEB calculations of the reduced structure to minimize the computational load, whereas a $3 \times 1 \times 3$ supercell was used for calculations of the oxidized structure as this produces a cell similar in size.

Oxide-ion diffusion in the reduced structure

The first step in studying O_i mobility in the reduced phase is to identify and determine the energetically most stable symmetrically unique interstitial sites. In $\text{Ca}_2\text{AlMnO}_5$ (space group $Ibm2$), there are two interstitial sites lying in the (101) plane. We labelled these sites X and Y, respectively. Ionic relaxation of the structure with interstitial O on X or Y sites, denoted $O_{i,X}$ and $O_{i,Y}$, respectively, revealed that O is

energetically less stable on the Y site than the X site by 0.73 eV. This means that the excess oxygen atoms tend to occupy X sites, and consequently ion transport involves anions moving from one X site to a neighbouring X site. This result is reasonable because upon oxidation oxide ions occupy the equivalent of X sites in the oxidized structure, $\text{Ca}_2\text{AlMnO}_{5.5}$. Although the Y site is energetically less stable for an excess oxide ion, it can act as an intermediate site for a complex diffusion mechanism in the [001] direction, as will be discussed in the next section.

To identify possible pathways, we enumerated all elementary migration paths as shown in Fig. 3. Of the five elementary paths we found, there are three in the [100] direction (P_a^I , P_a^{II} , P_a^{III}) and two in the [001] direction (P_c^I , P_c^{II}). Oxide ions migrate along P_c^I and P_a^{III} by an interstitial mechanism, whereas along the other pathways migration occurs by an interstitialcy mechanism. The interstitialcy mechanism involves cooperative motion of multiple atoms such that an interstitial atom moves onto an adjacent regular site and an atom on the regular site moves onto another interstitial site.

The calculated migration energy barriers for the different paths are listed in Table 2. For oxygen migration parallel to the c axis, the migration energy barriers of paths P_c^I and P_c^{II} are 0.58 eV and 0.25 eV, respectively. For oxygen migration parallel to the a axis, the migration energy barrier of path P_a^I was found to be the lowest of the three paths.

By connecting these elementary paths in different ways, four possible paths contributing to long-range diffusion are obtained, as summarized in Table 3. Of these, paths P_c^I and P_a^I have been considered in previous work on BM oxide $\text{SrCoO}_{2.5}$.¹² To the best of our knowledge, our study is the first to consider the other two paths. The results in Table 3 show that path P_c^I has the lowest migration energy barrier, at 0.58 eV. This value is within the range 0.4 eV to 0.8 eV that has been reported for many perovskite oxides used as SOFC cathodes.⁶ This value is also similar to those reported for $\text{SrCoO}_{2.5}$.¹² The second-lowest energy path is a complex pathway composed of paths P_a^{III} and P_c^{II} , which has a migration energy barrier of 0.98 eV (i.e., the height of the P_c^{II} peak, which corresponds to the sum of the energy of the P_a^{III} - P_c^{II} midpoint, $\text{O}_{i,Y}$, at 0.73 eV and P_c^{II} energy barrier of 0.25 eV). This value is 0.40 eV higher than that of path P_c^I .

Figure 4 shows the NEB images and corresponding minimum energy profile along the path P_c^I . The excess oxide ion is initially bonded to two aluminum atoms (Al_A and Al_C). As the excess oxide ion moves in the [001] direction, the O_i-Al_C distance increases, and conversely, the O_i-Al_B distance decreases, as illustrated in Fig. 4(b). As the O_i atom continues to migrate, the O_i-Al_A distance remains unchanged, suggesting that the Al_A atom acts as a pivot around which the O_i atom rotates. A similar mechanism has been reported in some other perovskite oxides, for example, $Ba_{0.5}Sr_{0.5}Co_{1-x}Fe_xO_{2.5}$,⁹ $SrCrO_{3-\delta}$ ¹¹ and $La_{1-x}Sr_xFeO_{3-\delta}$.³²

Figure 5 shows a schematic of the second-lowest energy pathway. This pathway is composed of three paths, P_a^{III} , P_c^{II} and P_a^{III} . First, the excess oxide ion, O_A , moves from an X site to a Y site. Next, O_A moves onto the Z site and the original O_B atom is pushed towards a neighbouring Y site. Lastly, the O_B atom continues migrating to its nearest neighbouring X site. The saddle point energy corresponds to when O_A passes between the two neighbouring Al atoms. This produces a large distortion to the crystal structure, so that the migration energy barrier of this pathway is larger than that of path P_a^I .

Oxide-ion diffusion in the oxidized structure

Next we examine oxygen diffusion in the oxidized phase. Since the movement of an O atom toward neighbouring vacant sites is equivalent to the movement of a vacancy in the opposite direction, the transport mechanism in this case is a simple vacancy hopping mechanism. Prior to connecting possible migration pathways, we identified the unique oxygen sites as shown in Fig. 6. Labels X (X'), Y (Y') and Z (Z') represent the oxygen sites in AlO_6 , Ca and MnO_6 layers, respectively. X and X' sites are symmetrically equivalent, but we assigned them different labels in order to distinguish different path directions, namely jumps from an X site to X site, X site to X' site, and X' site to X' site.

We performed first-principles calculations to determine the most energetically favourable site for oxide-ion vacancy formation. A vacancy on the X site, $v_{O,X}$, was found to have the lowest energy, with the $v_{O,Y}$, $v_{O,Z}$ and $v_{O,Z'}$ having energies relative to that of $v_{O,X}$ of 0.33 eV, 1.04 eV and 1.17 eV, respectively. This result is reasonable

because the straight-chain of X sites corresponds to the vacancy channel in the reduced phase. The large formation energies for vacancies on Z (Z') sites relative to those on X (X') sites indicate that oxygen vacancies in the AlO_6 layers are energetically less stable and thus diffusion of vacancies parallel to the b axis is unlikely.

We performed NEB calculations for the six possible paths identified in the oxidized structure. Of the six elementary paths, there is one in the $[100]$ direction (Q_a^I), one in the $[001]$ direction (Q_c^I) and in the $[010]$ direction ($Q_b^I, Q_b^{II}, Q_b^{III}, Q_b^{IV}$). As can be seen in Table 4, the energy barriers for oxygen vacancy diffusion parallel to the b axis are higher than 1.33 eV. In contrast, the barriers along paths Q_a^I and Q_c^I are almost identical in magnitude and lower than those of the other two paths, Q_b^I and Q_b^{II} . Paths Q_a^I and Q_c^I are thus the most energetically favourable, suggesting that diffusion is predominantly two-dimensional and occurs within AlO_4 layers.

Paths Q_a^I and Q_c^I are illustrated in Fig. 7. The oxygen atom migrates from X site to X site, and X' site to X' site, in an arc around an Al atom. The atoms neighbouring the vacancies remain at almost identical positions, but the neighbouring oxygen atoms shift slightly toward the vacancy. This displacement results in slightly distorted O–Al–O bonds similar to those in the reduced state. The small distortion is consistent with the small migration energy barriers of paths Q_a^I and Q_c^I . The slight difference in migration energy barriers between paths Q_a^I and Q_c^I is a result of lattice parameter a being slightly shorter in the case of the latter.

Anisotropy of oxide-ion diffusion

Oxide-ion diffusion in $\text{Ca}_2\text{AlMnO}_{5+\delta}$ is anisotropic, as expected from its anisotropic structure. In the reduced structure of $\text{Ca}_2\text{AlMnO}_5$, an excess oxide ion diffuses with a migration energy barrier of 0.58 eV through the vacancy channel, i.e., one-dimensionally, which is also the case for a variety of BM oxides reported in the literature.^{5,12} The excess oxide ion was found to be able to cross AlO_4 chains in the direction perpendicular to this via an interstitialcy diffusion mechanism with a migration energy barrier of 0.98 eV. This value is substantially lower than that in the literature for another interstitialcy diffusion mechanism.¹² This new pathway suggests

that two-dimensional diffusion may occur at high temperature or under a strong electric field, noting that the electrochemical potential of mobile O^{2-} changes as a function of temperature and electrical potential. In contrast, in the oxidized phase, $Ca_2AlMnO_{5.5}$, oxygen vacancies are found to migrate within AlO_4 layers with a migration energy barrier of about 0.6 eV in the [100] and [001] directions.

Our results reveal that a large migration energy barrier exists between O sites in Mn–O layers parallel to the b axis in the oxidized structure. Formation of an oxygen vacancy in an MnO_6 layer requires 1.00 eV and the migration energy barrier of this vacancy is 1.33 eV, indicating that diffusion in the [010] direction is essentially blocked by the transition-metal layer. These results thus indicate that, unlike in isotropically structured cubic perovskites, oxide-ion diffusion in the oxidized structure of $Ca_2AlMnO_{5.5}$ is two-dimensional, consistent with reports in the literature.⁶

Conclusions

We performed first-principles calculations to investigate the oxide-ion migration mechanism in brownmillerite-type Ca_2AlMnO_5 and $Ca_2AlMnO_{5.5}$. Oxygen transport via interstitial and vacancy diffusion mechanisms in both structures was demonstrated along different crystallographic pathways. The results suggest that in Ca_2AlMnO_5 , diffusion is one-dimensional, whereas in $Ca_2AlMnO_{5.5}$ it is two-dimensional. The low migration energy barrier of the interstitialcy mechanism in the case of the reduced structure suggests that two-dimensional diffusion in Ca_2AlMnO_5 is more rapid at high temperature than has previously been assumed. These insights into the relationship between oxide-ion diffusion and crystal structure of BM oxide $Ca_2AlMnO_{5+\delta}$, particularly in quantifying the anisotropy, are expected to inform the development of epitaxial thin films of this and related materials for electrochemical and electronic applications.

CRediT authorship contribution statement

Ushio Matsumoto: Investigating, Writing – Original Draft. Akihide Kuwabara: Conceptualization, Project Administration. Craig A. J. Fisher: Writing – Review and Editing. Hiroki Moriwake: Supervision. Isao Tanaka: Supervision, Writing – Review and Editing.

Conflicts of interest

The authors have declared no conflict of interest.

Acknowledgements

This work was supported by Cross-ministerial Strategic Innovation Promotion Program (SIP) “Energy systems toward a decarbonized society” from the Japan Science and Technology Agency (JST) and JSPS KAKENHI Grant Numbers JP19H05792 and JP 21H04621.

References

- 1 H. Jeon, W. S. Choi, M. D. Biegalski, C. M. Folkman, I. C. Tung, D. D. Fong, J. W. Freeland, D. Shin, H. Ohta, M. F. Chisholm and H. N. Lee, *Nature Materials*, 2013, **12**, 1057–1063.
- 2 H. Jeon, W. S. Choi, J. W. Freeland, H. Ohta, C. U. Jung and H. N. Lee, *Advanced Materials*, 2013, **25**, 3651–3656.
- 3 G. Corre, G. Kim, M. Cassidy, J. M. Vohs, R. J. Gorte and J. T. S. Irvine, *Chemistry of Materials*, 2009, **21**, 1077–1084.
- 4 H. Ullmann, N. Trofimenko, F. Tietz, D. Stöver and A. Ahmad-Khanlou, *Solid State Ionics*, 2000, **138**, 79–90.
- 5 R. H. E. van Doorn and A. J. Burggraaf, *Solid State Ionics*, 2000, **128**, 65–78.
- 6 C. Ling, R. Zhang and H. Jia, *ACS Applied Materials and Interfaces*, 2015, **7**, 14518–14527.
- 7 T. Motohashi, T. Ueda, Y. Masubuchi and S. Kikkawa, *Journal of Physical Chemistry C*, 2013, **117**, 12560–12566.
- 8 W. S. Choi, H. Jeon, J. H. Lee, S. S. A. Seo, V. R. Cooper, K. M. Rabe and H. N. Lee, *Physical Review Letters*, 2013, **111**, 097401.
- 9 H. Shiiba, C. L. Bishop, M. J. D. Rushton, M. Nakayama, M. Nogami, J. A. Kilner and R. W. Grimes, *Journal of Materials Chemistry A*, 2013, **1**, 10345–10352.
- 10 C. A. Fuller, Q. Berrod, B. Frick, M. R. Johnson, S. J. Clark, J. S. O. Evans and I. R. Evans, *Chemistry of Materials*, 2019, **31**, 7395–7404.

- 11 P. V. Ong, Y. Du and P. v. Sushko, *Journal of Physical Chemistry Letters*, 2017, **8**, 1757–1763.
- 12 C. Mitra, T. Meyer, H. N. Lee and F. A. Reboredo, *Journal of Chemical Physics*, 2014, **14**, 084710.
- 13 J. Lim and J. Yu, *Physical Review B*, 2018, **98**, 085106.
- 14 Q. Zhang, X. He, J. Shi, N. Lu, H. Li, Q. Yu, Z. Zhang, L. Q. Chen, B. Morris, Q. Xu, P. Yu, L. Gu, K. Jin and C. W. Nan, *Nature Communications*, 2017, **8**, 104.
- 15 T. Motohashi, Y. Hirano, Y. Masubuchi, K. Oshima, T. Setoyama and S. Kikkawa, *Chemistry of Materials*, 2013, **25**, 372–377.
- 16 T. Motohashi, T. Ueda, Y. Masubuchi, M. Takiguchi, T. Setoyama, K. Oshima and S. Kikkawa, *Chemistry of Materials*, 2010, **22**, 3192–3196.
- 17 T. Baidya, M. S. Hegde and J. Gopalakrishnan, *Journal of Physical Chemistry B*, 2007, **111**, 5149–5154.
- 18 P. E. Blöchl, *Physical Review B*, 1994, **50**, 17953–17979.
- 19 G. Kresse and J. Hafner, *Physical Review B*, 1993, **47**, 558–561.
- 20 G. Kresse and J. Furthmüller, *Physical Review B - Condensed Matter and Materials Physics*, 1996, **54**, 11169–11186.
- 21 J. P. Perdew, K. Burke and M. Ernzerhof, *Physical Review Letters*, 1996, **77**, 3865–3868.
- 22 J. P. Perdew, K. Burke and M. Ernzerhof, *Physical Review Letters*, 1997, **78**, 1396–1396.
- 23 H. J. Monkhorst and J. D. Pack, *Physical Review B*, 1976, **13**, 5188–5192.
- 24 M. Cococcioni and S. de Gironcoli, *Physical Review B - Condensed Matter and Materials Physics*, 2005, **71**, 035105.
- 25 S. Nosé, *The Journal of Chemical Physics*, 1984, **81**, 511–519.
- 26 W. H. Hoover, *Physical Review A*, 1985, **31**, 1695–1697.
- 27 G. Henkelman, B. P. Uberuaga and H. Jónsson, *Journal of Chemical Physics*, 2000, **113**, 9901–9904.
- 28 K. Momma and F. Izumi, *Journal of Applied Crystallography*, 2011, **44**, 1272–1276.
- 29 H. M. Palmer, A. Snedden, A. J. Wright and C. Greaves, *Chemistry of Materials*, 2006, **18**, 1130–1133.
- 30 A. J. Wright, H. M. Palmer, P. A. Anderson and C. Greaves, *Journal of Materials Chemistry*, 2002, **12**, 978–982.
- 31 G. Saito, Y. Kunisada, K. Hayami, T. Nomura and N. Sakaguchi, *Chemistry of Materials*, 2017, **29**, 648–655.
- 32 A. M. Ritzmann, A. B. Muñoz-García, M. Pavone, J. A. Keith and E. A. Carter, *Chemistry of Materials*, 2013, **25**, 3011–3019.

Tables

Table 1 Lattice parameters of $\text{Ca}_2\text{AlMnO}_5$ and $\text{Ca}_2\text{AlMnO}_{5.5}$.

Compound	Method	a (Å)	b (Å)	c (Å)
$\text{Ca}_2\text{AlMnO}_5$	Experiment ^a	5.4626	14.9532	5.2314
	DFT ^b	5.5228	15.1641	5.2760
	Present work	5.501	14.79	5.250
$\text{Ca}_2\text{AlMnO}_{5.5}$	Experiment ^c	5.2860	29.5334	5.4027
	DFT ^b	5.3035	29.5476	5.4310
	Present work	5.280	29.12	5.390

^a Ref. 30; ^b ref. 31; ^c ref. 29.

Table 2 Calculated migration energy barriers, E_m , and the corresponding diffusion mechanisms in $\text{Ca}_2\text{AlMnO}_5$ for different elementary paths.

Path	Diffusion mechanism	E_m (eV)
P_c^I	Interstitial	0.58
P_c^{II}	Interstitialcy	0.25
P_a^I	Interstitialcy	1.80
P_a^{II}	Interstitialcy	1.10
P_a^{III}	Interstitial	0.96

Table 3 Oxygen migration pathways and corresponding energy barriers, E_m , in $\text{Ca}_2\text{AlMnO}_5$.

Direction	Pathway	E_m (eV)
[001]	P_c^I	0.58
	$P_a^{III} - P_c^{II} - P_c^{II} - P_a^{III}$	0.98
[101]	$P_a^{III} - P_c^{II} - P_a^{III}$	0.98
[100]	P_a^I	1.80

Table 4 Oxygen migration paths and corresponding energy barriers, E_m , relative to $\nu_{0,X}$ in $\text{Ca}_2\text{AlMnO}_{5.5}$.

Direction	Path	E_m (eV)	
		Present work	Previous work
[001]	$Q_c^I: X \rightarrow X$	0.56	0.62 ^a
[100]	$Q_a^I: X' \rightarrow X'$	0.55	0.60 ^a
$[\bar{1}11]$	$Q_b^I: X \rightarrow Y$	0.96	
$[\bar{1}1\bar{1}]$	$Q_b^{II}: X' \rightarrow Y$	0.70	
$[11\bar{1}]$	$Q_b^{III}: Y \rightarrow Z$	1.33	
[111]	$Q_b^{IV}: Y \rightarrow Z'$	1.67	

^a Ref 6.

Figures

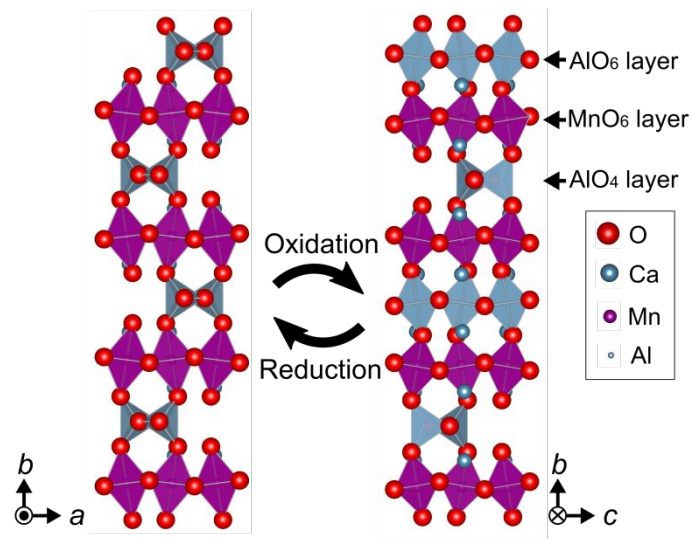


Figure 1 Crystal structures of brownmillerite $\text{Ca}_2\text{AlMnO}_5$ (left) and $\text{Ca}_2\text{AlMnO}_{5.5}$ (right). Mn and Al octahedra are purple and blue, respectively.

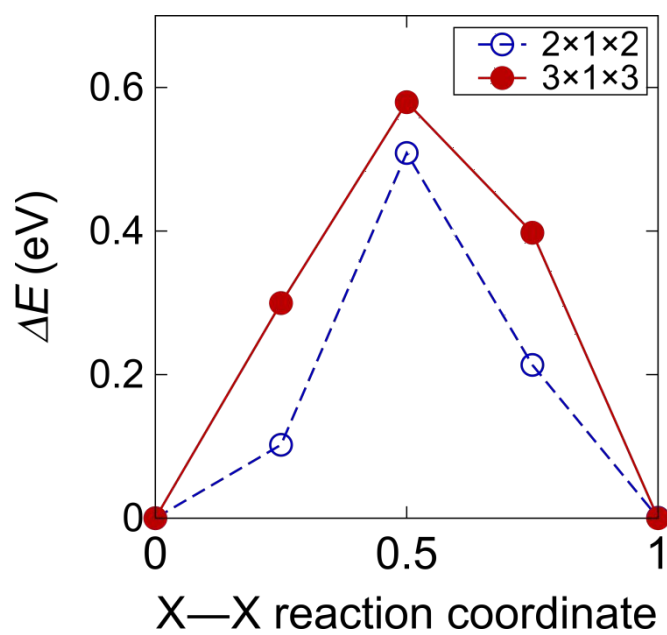


Figure 2 Energy difference, ΔE , of an excess oxide-ion migration in $2 \times 1 \times 2$ and $3 \times 1 \times 3$ supercells of $\text{Ca}_2\text{AlMnO}_5$.

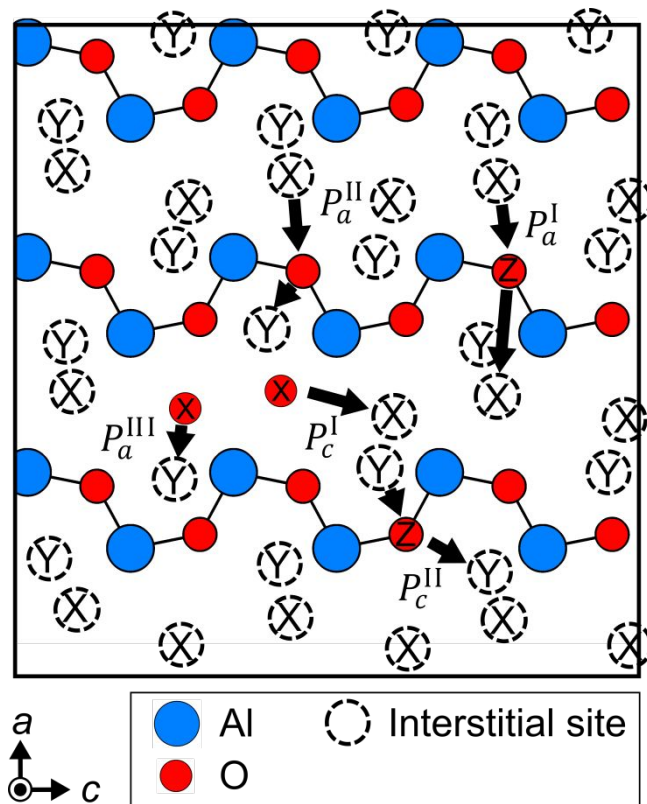


Figure 3 Elementary paths for oxygen diffusion in $\text{Ca}_2\text{AlMnO}_5$ within an AlO_4 layer. Symbols X and Y represent two symmetrically unique interstitial sites and Z represents an O3 site. Black arrows indicate the direction of oxygen migration.

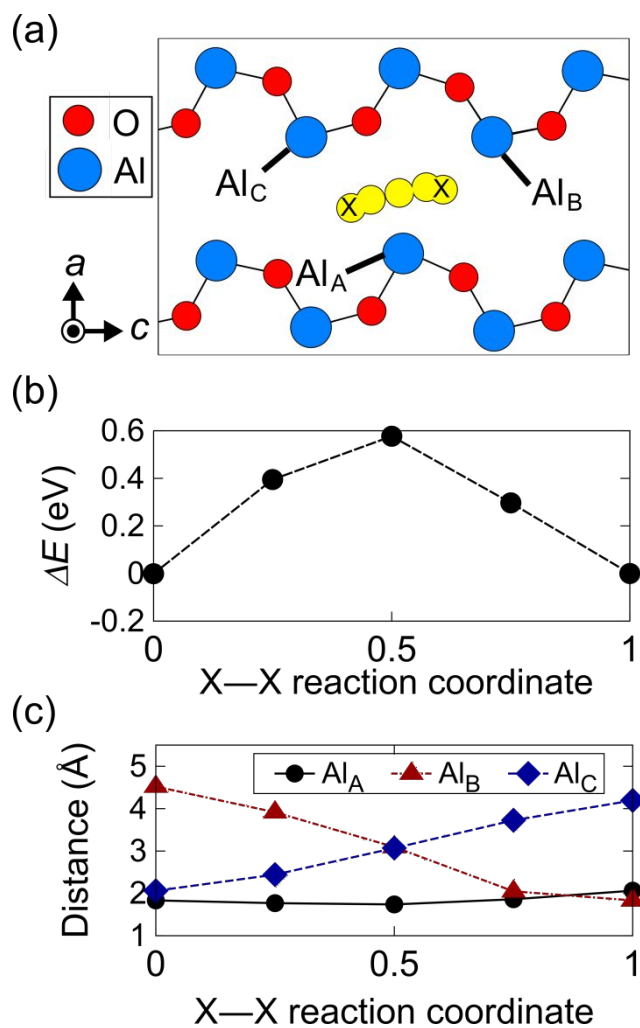


Figure 4 Excess oxide-ion migration along path P_c^I in an AlO₄ layer of Ca₂AlMnO₅: (a) schematic diagram of the interstitial mechanism, (b) calculated energy difference, ΔE , along the path, (c) distances between the excess O ion and Al ions along the path. In (a), light blue, red and yellow circles represent Al, lattice O and excess O atoms, respectively. Symbol X represents a $4b$ interstitial site.

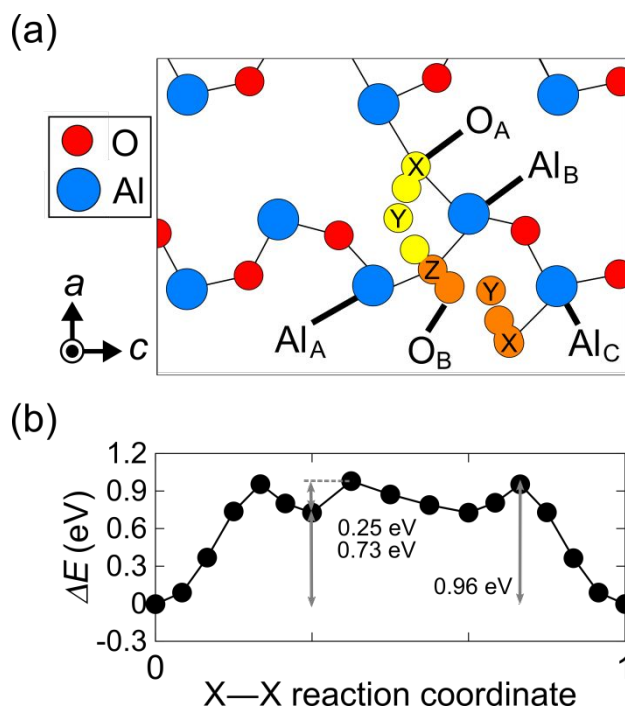


Figure 5 (a) Pathway $P_a^{\text{III}} - P_c^{\text{II}} - P_a^{\text{III}}$ and (b) the corresponding energy difference, ΔE , during oxide-ion migration in an AlO_4 layer of $\text{Ca}_2\text{AlMnO}_5$. In (a), light blue, red, yellow, and orange circles represent Al, lattice O, excess O and mobile O atoms, respectively. Symbols X and Y represent two symmetrically unique interstitial sites and Z represents an O3 site.

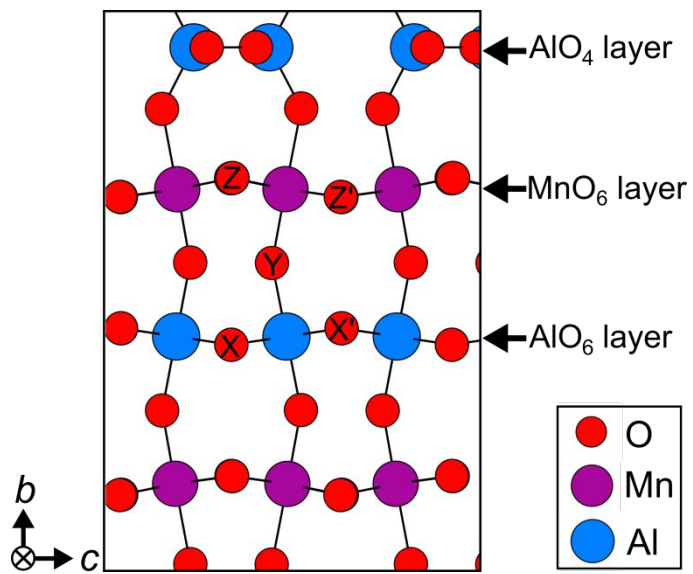


Figure 6 Crystal structure of $\text{Ca}_2\text{AlMnO}_{5.5}$ viewed down $[1\bar{0}1]$. Here, symbols X, X', Y, Z and Z' denote vacant sites.

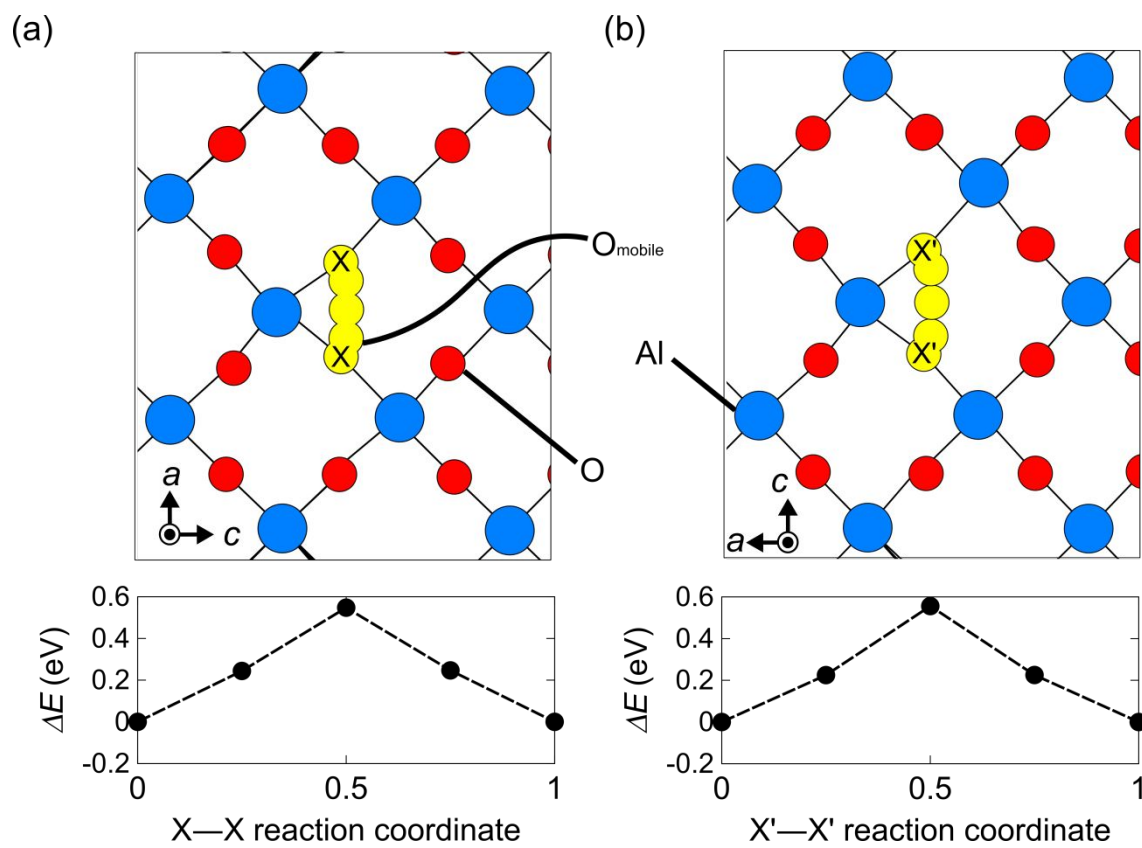


Figure 7 NEB images and calculated energy differences, ΔE , for O migration by a vacancy diffusion mechanism in an AlO_6 layer of $\text{Ca}_2\text{AlMnO}_{5.5}$ in the (a) [100] and (b) [001] directions. In the upper panels, light blue, red and yellow circles denote Al, lattice O and mobile O atoms, respectively. Symbols X and X' represent O1 site.